Experimental investigations and damage growth modeling of EN-AW 2024 aluminum alloy under LCF loading accounting creep pre-deformation

A. Tomczyk[1], A. Seweryn[2]

[1] Faculty of Mechanical Engineering, Białystok University of Technology, Poland (corresponding author)

[2] Faculty of Mechanical Engineering and Ship Technology, Gdańsk University of Technology, Poland

Abstract: This article presents the results of experimental tests of creep rupture and of low-cycle fatigue (LCF) of EN-AW 2024 aluminum alloy devoid of damage and having preliminary damage. The preliminary damage was dealt in the process of creep at elevated temperature 100°C, 200°C and 300°C until achievement of two different strain values at each temperature. Samples with preliminary damage were subjected to fatigue tests at room temperature. Based on the results of experimental tests, a simple damage accumulation model was proposed for creep at different temperatures. In this model, growth of the damage state variable was made dependent on the current value of axial stress and on growth of plastic strain. This model was also adapted for description of damage accumulation in the process of LCF for both as-received material and material with creep pre-deformation. In both cases, i.e. creep and LCF, the model's parameters were determined and it was experimentally verified.

Keywords: creep, low-cycle fatigue, creep and fatigue damage accumulation, pre-strain effect, damage evolution modeling.

Nomenclature

A_ω, n_ω – material parameters in the damage accumulation model

b,c – fatigue strength and ductility exponent

BSE – backscattered –electron imaging

C, D, m – material parameters

EBSD – electron backscatter diffraction

f – loading frequency

HAB – percentage of high angle boundaries

K, n – Ramberg-Osgood monotonic equation parameters

K', n' – Ramberg-Osgood cyclic equation parameters

LAB – percentage of low angle boundaries

LCF – low-cycle fatigue

N_f, N_{f_pred} – experimental and predicted number of cycles to failure respectively

R_ε – strain cycle asymmetry ratio

R–O – Ramberg-Osgood equation

SWT – Smith-Watson-Topper

t_t – transition time

t_{creep}, T_{creep} – time to creep-rupture and creep temperature respectively,

$\sigma_a^{mon}, \varepsilon_{ap}^{mon}$ – amplitude of monotonic stress and monotonic plastic strain respectively

ε_a, ε_{ae}, ε_{ap} – amplitude of total, elastic and plastic cyclic strain respectively

ε_{p1}, ε_{p2} – strain corresponds to the achievement of σ_{creep} value and at the moment of sample's rupture respectively

ε_s, ε_t – strain corresponds to the beginning of the secondary creep and to a certain strain from the tertiary stage

$\sigma_f', \varepsilon_f'$ – fatigue strength and ductility coefficient,

σ_{creep} – nominal stress value during creep process,

σ_a – cyclic stress amplitude

σ_t – nominal transition stress

σ – current nominal tensile stress value

σ_c – nominal failure stress for undamaged material

θ, θ_{av} – grain boundary misorientation angle and its averaged value respectively

ω_{creep}, ω_{LCF}, ω_{total} – damage state variable during creep and LCF processes and its total value

ω_{1k}, ω_{2k} – values of the damage state variable corresponding to strains ε_{p1} and ε_{p2} in the creep process

ω_{LCFp}, ω_{LCFk} – respectively, the initial and final value of damage state variable ω_{LCF} in the loading cycle

1. Introduction

The EN-AW 2024 alloy is a typical representative of aluminum alloys from the Al-Cu-Mg group. Its wide industrial applications were primarily determined by such properties as a favorable strength-to-weight ratio, high thermal and electrical conductivity, good fatigue resistance, easy mechanical workability or good corrosion resistance.[1-3] These features made the alloy widely used, among others, in the automotive, shipbuilding and aviation industries.[4-5] It is made of, for example, elements of the wing skins, fuselage bulk-heads and some elements in engine areas[6,7] like blades of low-pressure compressors.[8] Elements of this type can be subjected to both creep and fatigue processes. At the same time it should be remembered that often, cyclically varying loads are

preceded by mechanical or thermomechanical loads that are constant over time. This is of particular importance, for example, in cold expansion processes,[9-11] in problems of severe plastic deformation,[12,13] or in the case of structural components working in nuclear reactors.[14] A detailed analysis of the influence of preliminary creep on the fatigue life of aluminum alloy is presented in earlier papers.[15-18]

In the situation of consecutive creep and material fatigue, the fundamental problem becomes modeling of damage accumulation interactions caused by both processes. The first papers concerning a description of damage accumulation in creep problems involving simple loading states originate from continuous damage mechanics.[19,20] Many modern models are based on these propositions in order to generalize them to complex loading states.[21-26] The need to treat the damage state variable as a superposition of several components, among others, component associated with dislocation density and the component defined as the area fraction of cavitation under the creep constraint.[27-31]

In the case of fatigue processes, very often a single load cycle is considered and the damage accumulated in each cycle is summed up. The simplest method of summing assumes that the damage increases in the same way in each load cycle.[32-37] Modern models can be also far more complicated, which is why they can account for the influence of various factors on fatigue life and the material's damage state. The damage state variable is defined in different ways. Very often, it is defined by determining the share of the effective area in a component's entire cross-section or by using the Young's modulus of damaged and undamaged material.[38,39] In many papers,[40-42] this parameter is made dependent on total strain energy, accounting for the effect of average stresses, for example. A critical plane approach is often used based on the normal and share strain energy density parameter[43-45] or a special stress function is introduced, being a combination of normal and shear stresses.[46,47] The damage accumulation model is often made dependent only on inelastic hysteresis strain energy per cycle.[48-51] The well-known Smith-Watson-Topper (SWT) model[52-55] is widely used also, where the damage state variable is a combination of the total strain amplitude and maximum stresses in the loading cycle. In continuous damage mechanics, the damage growth process is often dependent on plastic deformation.[56-59]

This paper presents a model in which the increment of the damage state variable depends on the increments of plastic strains exactly and also on the nominal stresses. This model was used to predict the damage accumulation in both the creep process and LCF of the EN-AW 2024 aluminum alloy. It was introduced based on analysis of the results of experimental tests of the creep process at 100°C, 200°C and 300°C as well as LCF at room temperature of as-received material and of material with preliminary creep deformation.

2. Experimental tests of EN-AW 2024 aluminum alloy under uniaxial loading

2.1. Material, samples, testing equipment

Experimental investigations essentially concerned two areas: creep at elevated temperature,[60,61] LCF of material without preliminary strains and material with a certain history of thermomechanical loading.[17-18] The tested material was EN AW-2024 aluminum alloy in T3511 temper, in the form of extruded rods 16mm in diameter. The alloy's chemical composition is as follows (% weight): 0.13Si, 0.25Fe, 4.4Cu, 0.62Mn, 1.7Mg, 0.01Cr, 0.08Zn, 0.05Ti, 92.76Al. Full cylindrical samples with a diameter and gauge length of 6.5mm and 12.5mm, respectively, were used (Fig. 1). Samples intended for creep and fatigue tests were identical in shape with the exception of the grip section. In the case of samples used in creep tests, this part was threaded in order to ensure stable fastening at elevated temperature.

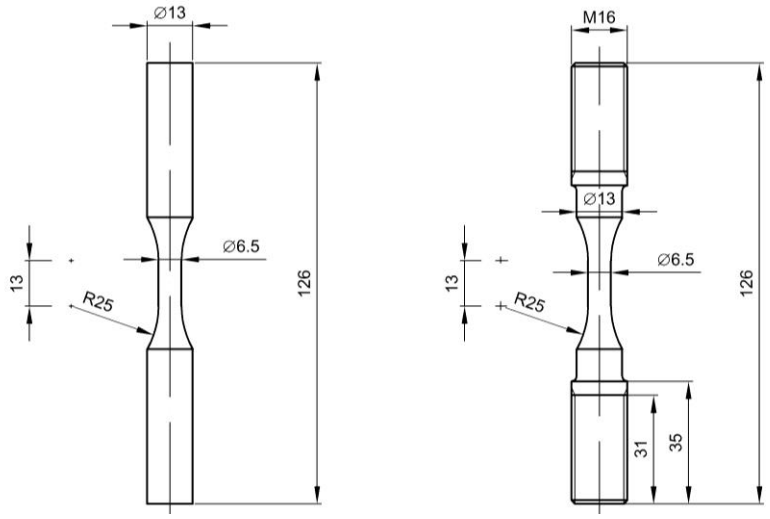

Fig. 1. Specimens used in creep and LCF tests (dimensions in mm)

In creep rupture tests, a uniaxial, four-column Kappa 100S creep testing machine with an electromechanical drive and loading range up to 100kN, manufactured by Zwick/Roell, was used. It enables the performance of creep rupture, creep, monotonic tensile, stress relaxation, as well as – if the appropriate instrumentation is applied – LCF tests. A special device allowing for measurement of strains in the sample while inside the furnace was used for strain measurement, with the application of devices intended for operation at room temperature.[62] In described tests, the holder cooperated with the Epsilon 3542-025M-025-HT1 extensometer, with a measurement base of 25 mm and range of ±12.5mm. Thermal loading was implemented using a three-zone Maytec furnace controlled by a dedicated Zwick/Roell controller. Sample temperature measurement was implemented by means of thermocouples. The whole system: creep tester – furnace – controller was

controlled by Testar Xpert II software. The test conditions were taken from the EN ISO 204 standard.[63]

LCF was implemented on a servo-hydraulic MTS 322 Test System with a force range of ±50kN. A dynamic INSTRON 2620-601 extensometer with a measurement base of 12.5 mm and ±5mm range was used for strain measurement. The LCF tests were based on the ASTM E606 standard.[64] It should be emphasized that both extensometers were calibrated before each single test with an accuracy of 0.001mm. During testing, with the extensometers mounted on the sample without load, the displayed value fluctuated to the fourth decimal place.

Investigations of the material's microstructure evolution were conducted using a Hitachi SU70 scanning electron microscope equipped with BSE and EBSD detectors. A square mesh of points, distant by 150 nm from one another, was used to EBSD mapping to obtain good representation of grains' shapes.

2.2. Experimental stress-strain and strain-time creep-rupture curves

Creep rupture tests were performed at temperatures 100°C, 200°C and 300°C for several different constant nominal stress values σ_{creep} at every temperature, given in Table 1 along with creep times.[60] In this paper, for the purposes of damage accumulation modeling (see Section 4.1), the creep process was presented in the nominal stress – nominal strain system (Fig. 2), not as customary in the nominal strain – creep time system.

Tab. 1. Nominal creep stress σ_{creep} and creep rupture time t_{creep} applied in creep rupture tests at different temperature $T_{creep.}$

T_{creep} [°C]	σ_{creep} [MPa]	t_{creep} [h]
100	524	20.35
	530	2.64
	532	0.45
200	229	89.05
	235	64.73
	256	24.25
	279	7.49
	297	2.69
300	51	135.83
	66	23.50
	75	17.93
	92	4.47
	123	0.82

Figure 2 shows the curves mentioned above, obtained for different σ_{creep} values. Plastic strain values ε_{p1} and ε_{p2} are also given. Strain ε_{p1} corresponds to the achievement of a constant value of nominal stress σ_{creep} during loading of the sample, and ε_{p2} is the permanent strain at the moment of the sample's rupture. The creep process is shown generally in the nominal stress – nominal strain system in Figure 1d. A characteristic regularity was observed in the creep-rupture process at 200°C and 300°C. In the case of σ_{creep} loads above a certain transitional value σ_t, corresponding to time t_t, the decrease in load during creep is accompanied by a strain increase at the moment of rupture (Fig. 1bc). However, for $\sigma_{creep}<\sigma_t$ this strain decreased as load value decreased and creep time increased. Such a regularity was also confirmed for 2124 alloy.[65]

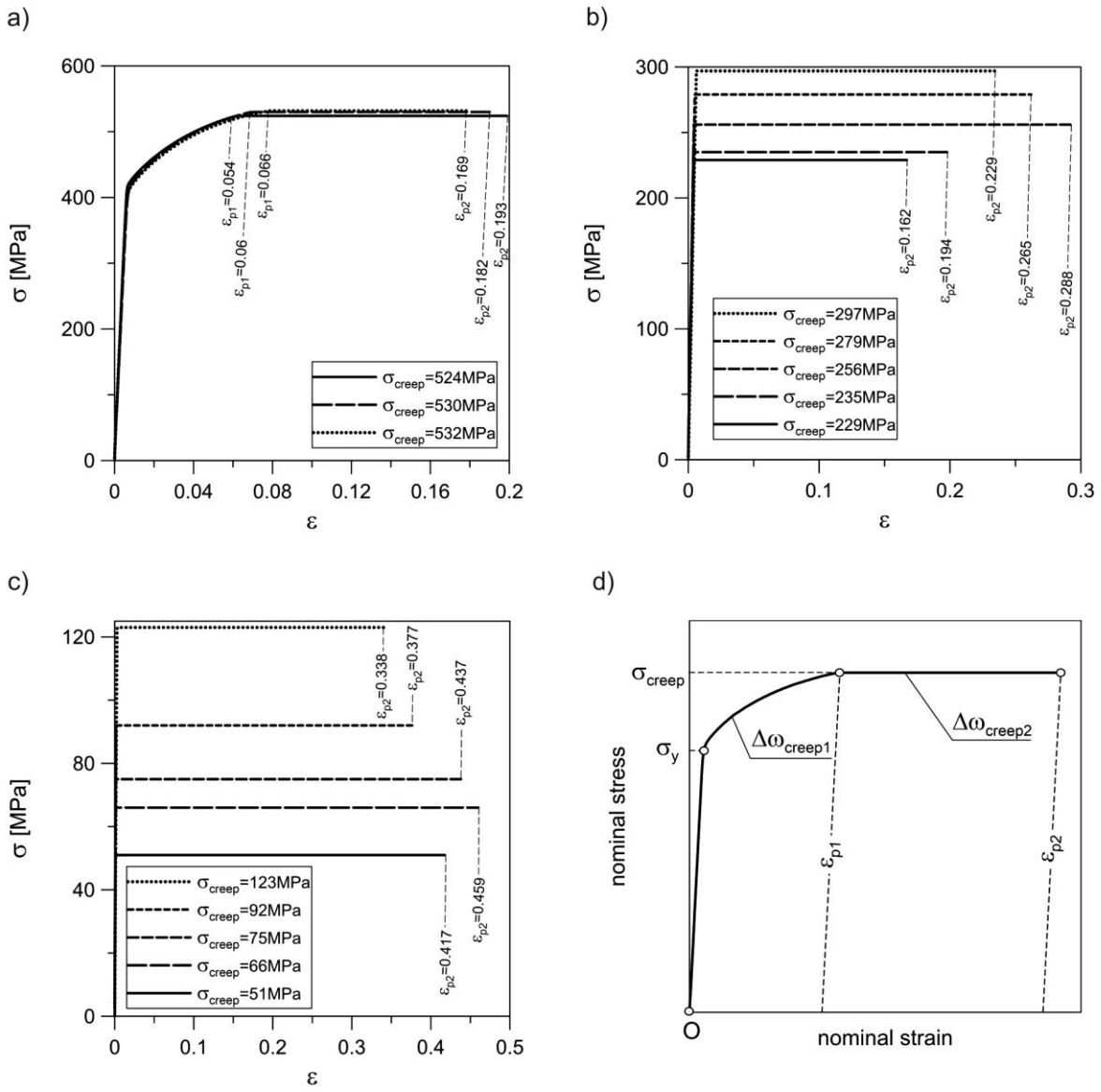

Fig. 2. Creep rupture curves in nominal stress – nominal strain coordinate system obtained at temperature: a) 100°C, b) 200°C, c) 300°C, and d) schematic representation of creep rupture curve.

The obtained creep rupture curves made it possible to determine the constant nominal stress value at which the pre-deformation process was performed and the two levels of this deformation. The first of them, ε_s, corresponded to the beginning of the stable stage of creep, while the second ε_t to a certain strain from the third stage. The pre-deformation process was performed at 100°C under stress σ_{creep}=530MPa until reaching ε_s=10% or ε_t=15%. For 200°C, σ_{creep}=279MPa and ε_s=0.6% or ε_t=2.3% were accepted, and for 300°C – σ_{creep}=92MPa, ε_s=0.4% or ε_t=2.3%. After reaching the set strain, the sample was unloaded and cooled in open air. In this way, the defined pre-deformation of samples' material was obtained and they were subsequently subjected to LCF loading.

2.3. Cyclically varying loading

Fatigue tests were performed at room temperature 21°C with a constant value of the total strain amplitude ε_a at a frequency of f=0.2Hz and with strain cycle asymmetry factor R_ε=–1. The following ε_a values were applied: 0.02, 0.01, 0.008, 0.005, 0.0035. A paper by Tomczyk and Seweryn[17] presents detailed results of these tests, in the form of the number of cycles to failure N_f, σ_a stress amplitude, and fatigue life curves according to the Manson-Coffin-Basquin proposition, among others:[66-68]

$$\varepsilon_a = \varepsilon_{ae} + \varepsilon_{ap} = \frac{\sigma_f'}{E}\left(2N_f\right)^b + \varepsilon_f'\left(2N_f\right)^c, \tag{1}$$

where ε_a, ε_{ae}, ε_{ap} is the amplitude of total, elastic and ductile strain respectively, $\sigma_f', \varepsilon_f'$ are the fatigue strength and ductility coefficients, b, c – the fatigue strength and ductility exponent.

In this paper, for the purposes of modeling damage accumulation in the LCF process (see Section 4.2), it is necessary to determine the parameters of the fatigue life curve for the LCF in the (Manson-Coffin) form:

$$\varepsilon_{ap} = \varepsilon_f'\left(N_f\right)^c, \tag{2}$$

In comparison to the original Manson-Coffin proposition, the $2N_f$ value was replaced here with the N_f value.

The parameters of equation (2) are given in Table 2. This table also includes values of the K factor and n exponent in the Ramberg-Osgood (R-O) equation for monotonic strain:[69]

$$\sigma_a^{mon} = K\left(\varepsilon_{ap}^{mon}\right)^n \tag{3a}$$

where $\sigma_a^{mon}, \varepsilon_{ap}^{mon}$ are monotonic stress and plastic strain amplitudes, and the K' factor and n' exponent in the R-O equation for cyclic strain:

$$\sigma_a = K'\left(\varepsilon_{ap}\right)^{n'} \tag{3b}$$

obtained based on a monotonic test of samples before and after pre-deformation. It should be noted here that both the K' factor and n' exponent in equation (3b) remained unchanged following pre-deformation, in contrast to the factors in the Manson-Coffin equation (2).

Tab. 2. Parameters of fatigue life curve and also monotonic and cyclic strain curves for as-received material and for material with different history of pre-deformation.

pre-deformation temperature [°C]	ε_s or ε_t [%]	ε_f'	c	monotonic		cyclic	
				K [MPa]	n	K' [MPa]	n'
as-received	–	0.046	–0.639	693	0.0790	1093	0.134
100	10	0.042	–0.793	629	0.0097	1134	0.123
	15	0.015	–0.752	645	0.0027	1256	0.123
200	0.6	0.062	–0.631	623	0.0458	1256	0.156
	2.3	0.373	–0.867	563	0.0420	761	0.107
300	0.4	0.786	–0.887	505	0.1119	493	0.098
	2.3	0.791	–0.815	473	0.1481	412	0.110

The greatest differences in values of the material's LCF characteristics following pre-deformation with respect to the initial material concern, above all, preliminary strains at 200°C and 300°C. This is linked to the microstructure's evolution as a result of loading at elevated temperature (see Section 3). Experimental results of the cyclic strain curve and their approximations by equation (3b) are shown in Figure 3. Also in this case, there are substantial differences in the values of the factor and exponent in this equation (Tab. 2). In the case of the material with pre-deformation at 100°C, there was a significant hardening in relation to the as-received material (Fig. 3a). It results from large values of initial deformations and the subsequent unloading of the material. The slightly elevated temperature effect was practically irrelevant here. On the other hand, in the case of pre-deformation at 300°C (Fig. 3c), the influence of temperature is clearly visible. There is a significant reduction of strength parameters here. It is the more pronounced the greater was the level of pre-deformation during creep. This is related to the evident process of recrystallization of the microstructure taking place here (see Section 3). This process takes place in aluminum alloys at a temperature of about 250°C, even with no mechanical loads. It becomes more effective in the event of external loads. The greater the value of the load at a given temperature, the more intense the recrystallization process takes place, the effect of which is shown in Figure 3c. A similar tendency was observed for monotonic curves.

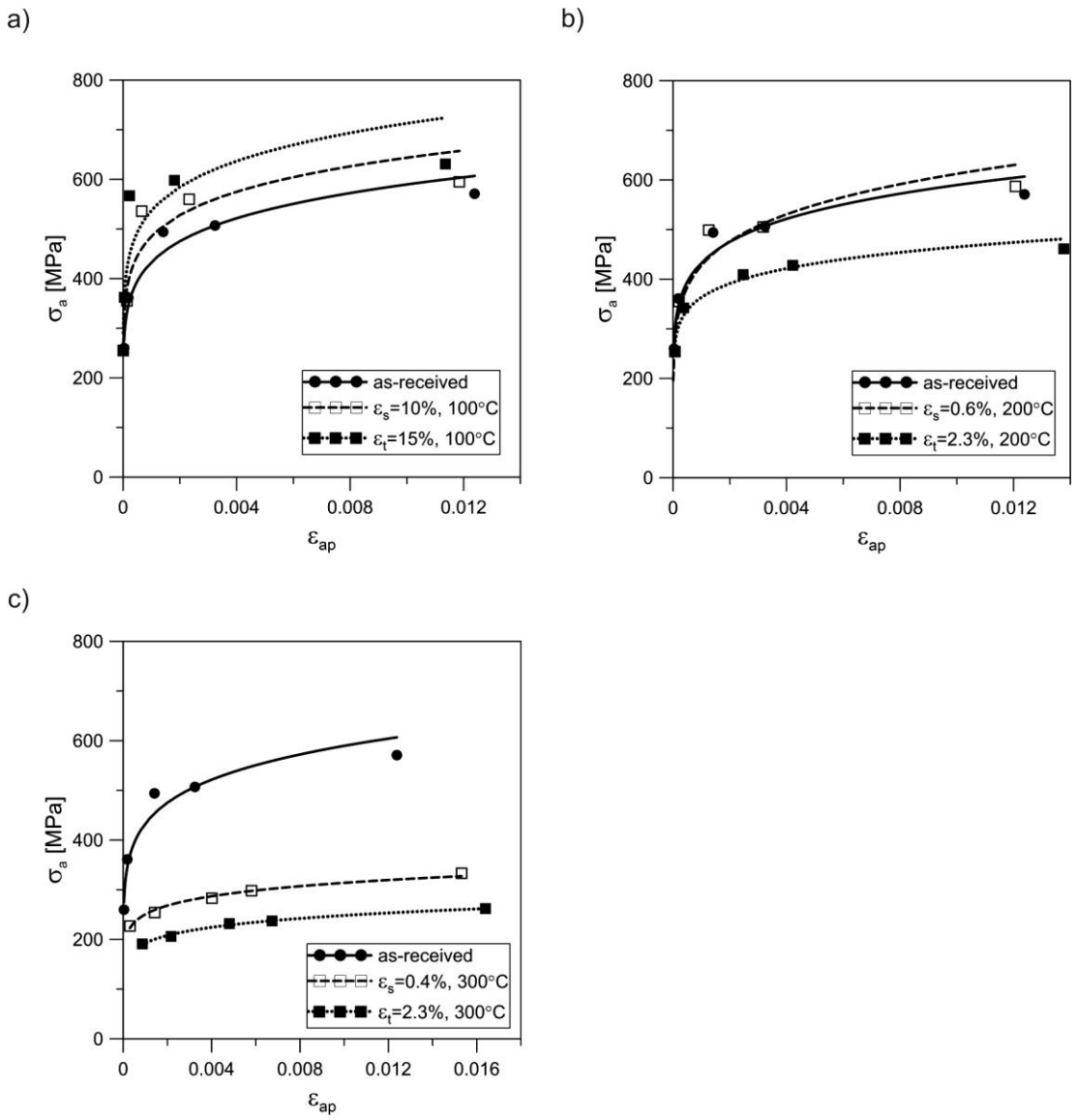

Fig. 3. Cyclic strain curves for different pre-deformation histories according to equation (3b) on the background on curves for as-received material: a) pre-deformation at 100°C, b) pre-deformation at 200°C, c) pre-deformation at 300°C

The LCF life curve corresponding to equation (1) is shown in Figure 4. For easier comparison of the charts, the same value ranges are applied on both axes and the experimental data are compared in Table 5. For the material with pre-deformation at 100°C, where purely mechanical hardening dominated, it was observed that the fatigue life significantly decreased compared to the as-received material in the entire load range. In the case of preliminary deformations at the temperature of 200°C and 300°C the material's fatigue life increases with respect to that of the as-received material in the area where plastic strains are dominant. This can be observed particularly clearly in the case of pre-deformations implemented during creep at 300°C. In the area where plastic strains are lowest, fatigue life deteriorates in comparison to the as-received material. Thus,

as can be seen, the recrystallization process (see Section 3) caused the deterioration of the monotonic characteristics, but the improvement of the fatigue life in the LCF range.

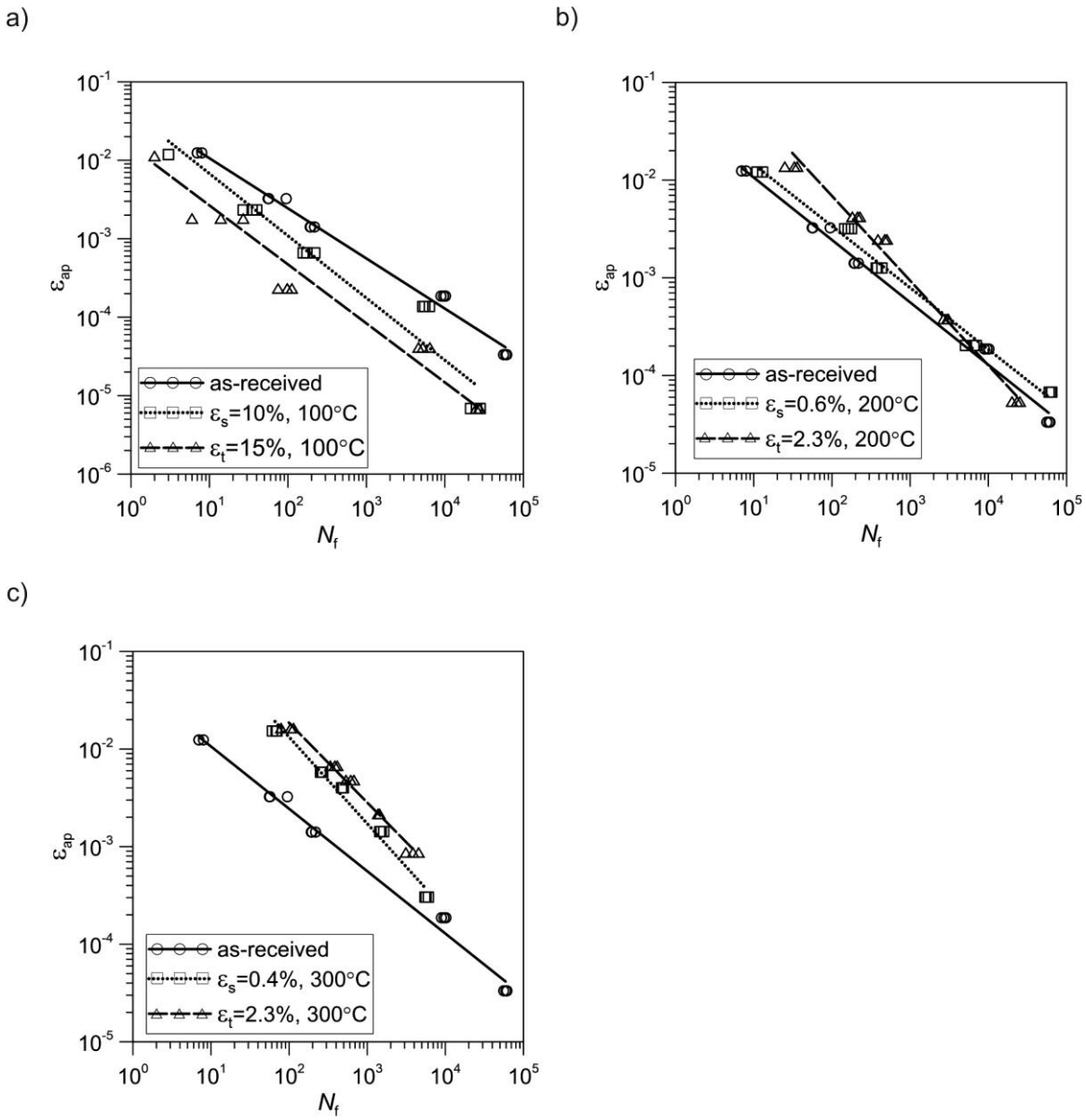

Fig. 4. Fatigue life curves described by equation (1) for different pre-deformation histories on the background of curves for as-received material: a) 100°C, b) 200°C, c) 300°C

3. Microstructure evolution caused by creep at elevated temperature

Prior studies show that, in the case of creep at 100°C, there are no distinct changes in the material's microstructure.[18] The only changes involve grain elongation and width reduction. In relation to the above, only samples after the creep process at 200°C and 300°C were analyzed in detail from the perspective of microstructure evolution. Three samples were investigated for each temperature. They were selected so that creep times differed significantly (Tab. 3).

Tab. 3. Nominal creep stress σ_{creep} and creep rupture time t_{creep} for samples used in microstructure evolution analysis together with sample symbols and basic quantities defining material microstructure.

sample symbol	T_{creep} [°C]	σ_{creep} [MPa]	t_{creep} [h]	*LAB* [%]	θ_{av} [°]	averaged grain size [μm]
200/01	200	229	89.05	95	14.2	1.56
200/02		256	24.25	92	7.4	1.45
200/03		297	2.69	78	7.3	1.17
300/01	300	51	135.83	91	7.7	1.74
300/02		75	17.93	86	9.9	1.69
300/03		123	0.82	86	11.1	1.57

Above all, tests using an EBSD detector were performed at the Faculty of Materials Science and Engineering of the Warsaw University of Technology. They were intended for obtaining a map of grain boundary misorientation following various thermomechanical loads (Figs 5,8). The area under analysis was the surface of the sample on its longitudinal plane of symmetry, in close proximity to the axis of symmetry, just under the surface of the post-creep fracture. The sample's axis of symmetry, simultaneously being the loading direction, is oriented horizontally on all pictures. Attention should be paid to the location of the tested area. First of all, this is the neck area, where the greatest strains occur. These strains are higher as the temperature of the test increase and σ_{creep} load decreases. On the other hand, the strain rate at this location is greater as load increases. In tandem, both parameters, i.e. strain value and rate, beside the value of temperature, are the main factors deciding the possibility of occurrence and intensity of the dynamic recrystallization process. Hence, we may be dealing with two "antagonistic" effects. This refers, for example, to cases of high strain values and low strain rates or vice versa.

Figure 5 shows a grain boundary misorientation map for samples following the creep process at 200°C for different σ_{creep} values. Here, large primary grains, elongated in the direction of the sample's axis, can clearly be observed. Boundaries with an angle of misorientation above 15° are marked in black. The gray color represents boundaries with a low angle of misorientation (LAB), i.e. 3-15°.The sample with the longest creep time (Fig. 5a) is characterized by a substantially developed substructure of boundaries of this type. Boundaries oriented consistently with the axis of grains and oriented randomly can be distinguished. In the case of the sample with the shortest creep time, LABs also form such substructures, however their density is clearly lower. For long creep times, partial recrystallization of the microstructure can also be observed. The new grains formed as a result of this recrystallization cause softening of the material.

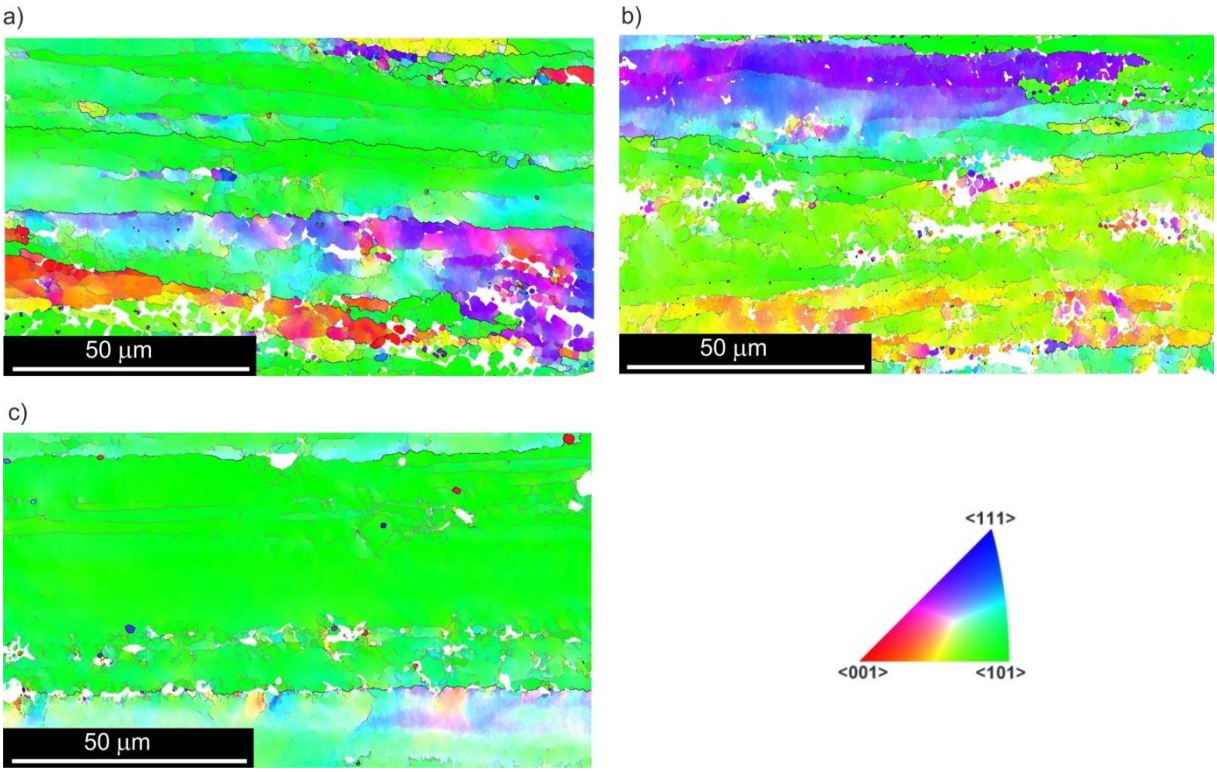

Fig. 5. Grain misorientation maps for samples following creep rupture tests at 200°C for different values of σ_{creep}: a) sample 200/01 (σ_{creep}=229MPa, t_{creep}=85.05h), b) sample 200/02 (σ_{creep}=256MPa, t_{creep}=24.25h), c) sample 200/03 (σ_{creep}=297MPa, t_{creep}=2.69h).

Clear growth of the fraction of low-angle boundaries (LAB) was observed as creep time t_{creep} increased and creep stress σ_{creep} decreased (Tab. 3). In the case of the sample with the longest creep time (t_{creep}=2.69h), this fraction amounted to 78%. For creep time t_{creep}=24.25h, it increased significantly, to 92%. A further increase of creep time to t_{creep}=89.05h caused only small growth of the fraction of LAB, i.e. to 95%. At the same time, the average angle of misorientation θ_{av} for creep times t_{creep}=2.69h and t_{creep}=24.25h remains essentially unchanged, whereas for creep time t_{creep}=89.05h, it increases nearly two-fold (Fig. 6). The presence of a peak in Figure 6b indicates the large fraction of low angle boundaries (θ≈3°). It should be noted that this situation only pertains to the case where t_{creep}=24.25h. For other creep times, the fraction of boundaries with the lowest misorientation angle is significantly lower. As creep time increases and the σ_{creep} value decreases, the fraction of these boundaries grows up to a certain value.

As shown by θ angle distributions for longer creep times, the fraction of LABs again decreases. At the same time, the peaks in Figures 6a and 6c are much wider, and so the fraction of boundaries from the 3-10° range is significant here. Growth in the fraction of high-angle boundaries is also characteristic for a longer time of creep until failure (Fig. 6a). This may indicate a continuous character of the dynamic recrystallization process. The above may decide the increase in strain at failure only for σ_{creep} stresses above the value of σ_t (see Section 2.2). Below this value,

strain at failure decreases once more. However, more detailed investigations of the microstructure should be conducted.

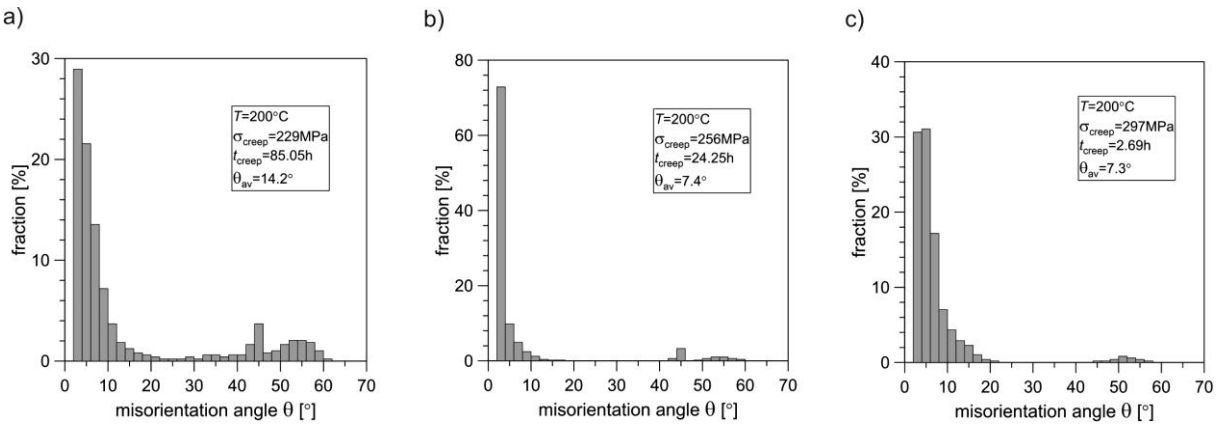

Fig. 6. Distribution of grain boundaries misorientation angles after creep rupture tests at 200°C for different values of σ_{creep}: a) sample 200/01, b) sample 200/02, c) sample 200/03.

As shown by θ angle distributions for longer creep times, the fraction of LABs again decreases. At the same time, the peaks in Figures 6a and 6c are much wider, and so the fraction of boundaries from the 3-10° range is significant here. Growth in the fraction of high-angle boundaries is also characteristic for a longer time of creep until failure (Fig. 6a). This may indicate a continuous character of the dynamic recrystallization process. The above may decide the increase in strain at failure only for σ_{creep} stresses above the value of σ_t (see Section 2.2). Below this value, strain at failure decreases once more. However, more detailed investigations of the microstructure should be conducted.

The grain size distribution analysis showed that an increase of the time of creep rupture increases the fraction of larger grains in the material's microstructure. To determine grain and subgrain sizes, an equivalent diameter corresponding to the diameter of a circle with an area identical to the area of the studied grain was used. For statistics, areas surrounded by closed boundaries with an angle of disorientation no lower than 3° were used. In every case, the size of over 50% of all grains is less than 2μm. Average grain sizes for individual loads are given in Table 3.

Figure 7 shows photographs taken in backscatter electron mode (BSE). Precipitates of large size containing Cu (light objects) are clearly visible on the boundaries of fibrous grains. Finer precipitates are distributed randomly. A longer time of elevated temperature under load caused the appearance of a larger number of precipitates with larger sizes (Figs 7b and 7c). The interface between a precipitate, particularly a coarse-grained one situated on a grain boundary, and the matrix is typically the location of microcrack initiation.

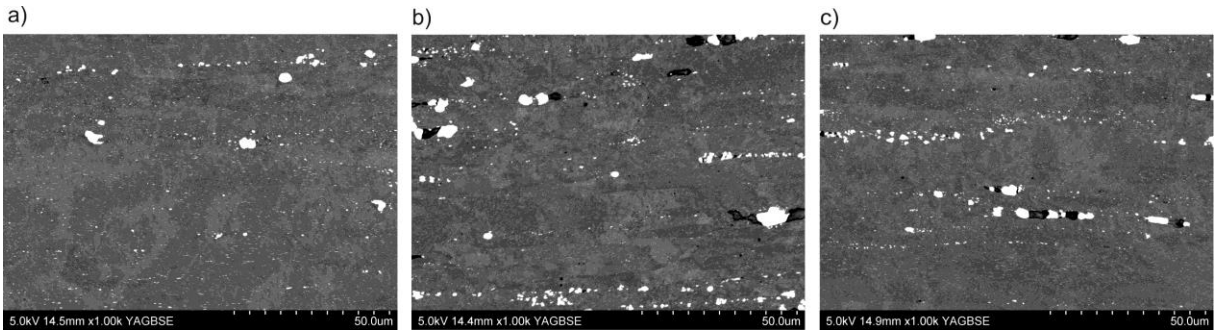

Fig. 7. View of material microstructure after creep rupture tests at 200°C made in BSE mode: a) sample 200/01, b) sample 200/02, c) sample 200/03.

In the case of creep rupture tests at 300°C, the material's microstructure (Fig. 8) exhibits significant differences in comparison to the microstructure obtained during creep at 200°C. Refinement resulting from the recrystallization process can clearly be seen, particularly for long times of exposure to elevated temperature (Fig. 8a). Here, a very well developed structure of LABs (gray lines) is visible. The shape of grains is similar to equiaxial. The formation of these grains is the result of regrouping and annihilation of dislocations and is typical for materials with a high stacking fault energy (SFE).[70] In the case of higher load values, subgrains are elongated in the direction of the load's action (Figs 8a and 8b).

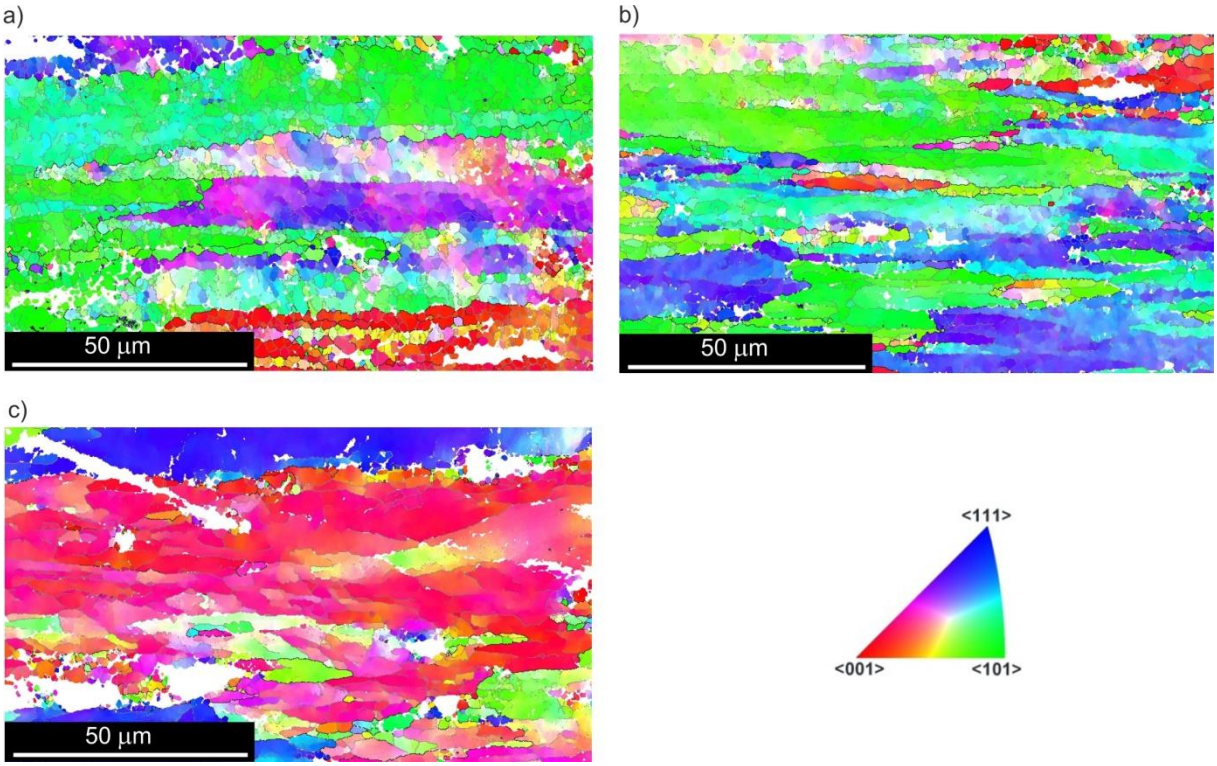

Fig. 8. Grain misorientation maps for samples following creep rupture tests at 200°C for different values of σ_{creep}: a) sample 300/01 (σ_{creep}=51MPa, t_{creep}=135.83h), b) sample 300/02 (σ_{creep}=75MPa, t_{creep}=17.93h), c) sample 300/03 (σ_{creep}=123MPa, t_{creep}=0.82h).

The distribution of grain boundary misorientation angles is very similar for longer creep times (Figs 9a and 9b). In the case of the shortest creep time (t_{creep}=0.82h), microstructure is characterized by a different distribution in terms of LAB (Fig. 9c). A lower fraction of boundaries with 3-5° angles was observed, however the peak is wider. Growth of the fraction of low-angle boundaries can be seen as t_{creep} time increases, however this growth is not as substantial as in the case of 200°C.

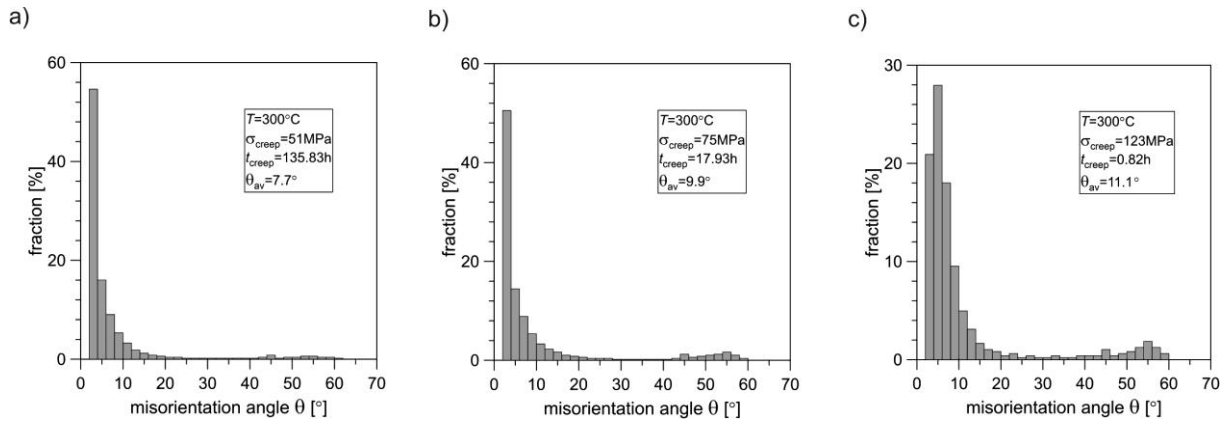

Fig. 9. Distribution of grain boundaries misorientation angles after creep rupture tests at 300°C for different values of σ_{creep}: a) sample 300/01, b) sample 300/02, c) sample 300/03.

It is worth noting that, for 300°C, the average disorientation angle θ_{av} decreases as creep until failure time increases, which is accompanied by a reduction in strain (Tab. 3, Fig. 9). A similar regularity was observed for 7475 alloy, and ultra-fine grains formed in 7474 alloy.[71] In contrast to the case of creep at 200°C, the fraction of high-angle boundaries (HAB) is greatest for the shortest times, and hence, for the highest strains. Both grain size distribution and average grain size are similar for all creep times (Tab. 3). It should be noted that at a temperature of about 240-270°C, recrystallization occurs in aluminum alloys. It is the more intense the greater the value of the creep loading. Thus, there is a situation in which the existing grains grow as a result of being exposed to an elevated temperature. On the other hand, new small grain sizes are created. At the temperature of 200°C, recrystallization takes place to a much smaller extent, hence the tendency of the average grain size to increase due to longer residence times at elevated temperature is more distinct here.

Observation in BSE mode reveals certain dependencies in the distribution of precipitates with respect to grain boundaries (Fig. 10). In the case of the longest creep time, fine precipitates are mostly distributed uniformly throughout the entire field of observation. Two fractions can be distinguished. Larger precipitates mainly occur on grain boundaries and smaller ones inside grains. In Figure 10, a tendency can be seen that in the case of a long creep time, there are more precipitates than in the case of shorter times. This is especially true of small precipitations, but in general the participation of all precipitates is clearly decreasing.

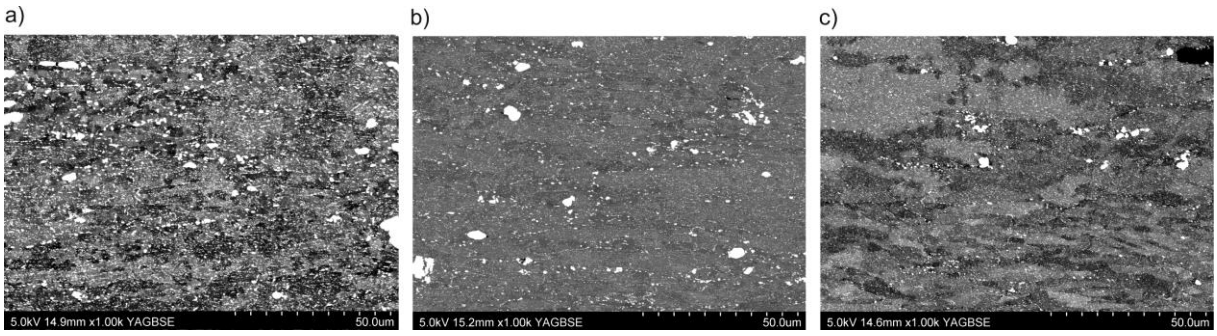

Fig. 10. View of material microstructure after creep rupture tests at 300°C made in BSE mode: a) sample 300/01, b) sample 300/02, c) sample 300/03.

Figure 7 shows the opposite tendency, i.e. there is less precipitation with longer stay times at elevated temperatures. These precipitates block the grain rotation process and their separation, thus improving the creep resistance. On the other hand in the case of fatigue loading, they can usually constitute the origin of crack initiation and lead to failure. This particularly applies to coarse-grained particles with sharp edges.

4. Modeling of the damage accumulation

4.1. Damage growth model for creep at elevated temperature

In the proposed theoretical model, it was accepted that damage accumulation in the creep until failure process depends on the axial stress value and the growth of plastic strains. When introducing the damage state variable ω_{creep}, the damage accumulation law was adopted in the form of:[72,60]

$$\mathrm{d}\omega_{\text{creep}} = \begin{cases} A_{\omega}\left(\dfrac{\sigma}{\sigma_{\text{c}}}\right)^{n_{\omega}} \mathrm{d}\varepsilon_{\text{p}} & \text{dla } \sigma > 0 \text{ i } \mathrm{d}\varepsilon_{\text{p}} > 0 \\ 0 & \text{dla } \sigma \le 0 \text{ lub } \mathrm{d}\varepsilon_{\text{p}} \le 0 \end{cases}, \tag{4}$$

where: A_{ω}, n_{ω} – material parameters independent of load value (but dependent on the material's microstructure), σ – current nominal tensile stress value, σ_{c} – nominal failure stress for undamaged material (also dependent on the material's microstructure).

The ω_{creep}=0 value signifies undamaged material while ω_{creep}=1 – total failure. Since it was assumed that damage accumulation is associated with plastic strains, damage does not increase in the linear-elastic range of the creep curve (Fig. 2d). The total accumulation of damage in the creep rupture process can be written as the sum of two components:

$$\omega_{\text{creep}} = \Delta\omega_{\text{creep1}} + \Delta\omega_{\text{creep2}}. \tag{5}$$

The first part ($\Delta\omega_{\text{creep1}}$) corresponds to the increase of the damage state variable within the stress range from the time when the material's yield point σ_{y} is reached until reaching of a constant force in the creep process corresponding to σ_{creep} stress. The second part ($\Delta\omega_{\text{creep2}}$) defines the increase of the damage metric from reaching of σ_{creep} stress until sample failure, which corresponds to failure stress σ_{c}. According to the damage accumulation law (3):

$$\Delta\omega_{\text{creep1}} = \int_0^{\omega_{1\text{k}}} \mathrm{d}\omega_{\text{creep1}} = \frac{A_\omega}{\sigma_{\text{c}}^{n_\omega}} \int_0^{\varepsilon_{\text{p1}}} \sigma^{n_\omega} \mathrm{d}\varepsilon_{\text{p}}, \tag{6}$$

$$\Delta\omega_{\text{creep2}} = \int_{\omega_{1\text{k}}}^{\omega_{2\text{k}}} \mathrm{d}\omega_{\text{creep2}} = A_\omega \left(\frac{\sigma_{\text{creep}}}{\sigma_{\text{c}}}\right)^{n_\omega} \int_{\varepsilon_{\text{p1}}}^{\varepsilon_{\text{p2}}} \mathrm{d}\varepsilon_{\text{p}}, \tag{7}$$

where: $\omega_{1\text{k}}$, $\omega_{2\text{k}}$ – values of the damage state variable corresponding to strains ε_{p1} and ε_{p2} in the creep process.

Assuming a strain hardening curve in the form of the plastic part of the Ramberg-Osgood equation (3a), equations (6) and (7) ultimately take the form of:

$$\Delta\omega_{\text{creep1}} = A_\omega \left(\frac{K}{\sigma_{\text{c}}}\right)^{n_\omega} \int_0^{\varepsilon_{\text{p1}}} \left(\varepsilon_{\text{p}}\right)^{nn_\omega} \mathrm{d}\varepsilon_{\text{p}} = \left(\frac{K}{\sigma_{\text{c}}}\right)^{n_\omega} \frac{A_\omega}{\left(nn_\omega + 1\right)} \left(\varepsilon_{\text{p1}}\right)^{\left(nn_\omega + 1\right)}, \tag{8}$$

$$\Delta\omega_{\text{creep2}} = A_\omega \left(\frac{\sigma_{\text{creep}}}{\sigma_{\text{c}}}\right)^{n_\omega} \left(\varepsilon_{\text{p2}} - \varepsilon_{\text{p1}}\right). \tag{9}$$

$$\omega_{\text{creep}}\left(\varepsilon_{\text{p}}\right) = \begin{cases} \left(\dfrac{K}{\sigma_{\text{c}}}\right)^{n_\omega} \dfrac{A_\omega}{\left(nn_\omega + 1\right)} \left(\varepsilon_{\text{p}}\right)^{\left(nn_\omega + 1\right)} & \text{dla} \quad \varepsilon_{\text{p}} \le \varepsilon_{\text{p1}} \\ \left(\dfrac{K}{\sigma_{\text{c}}}\right)^{n_\omega} \dfrac{A_\omega}{\left(nn_\omega + 1\right)} \left(\varepsilon_{\text{p1}}\right)^{\left(nn_\omega + 1\right)} + A_\omega \left(\dfrac{\sigma_{\text{creep}}}{\sigma_{\text{c}}}\right)^{n_\omega} \left(\varepsilon_{\text{p}} - \varepsilon_{\text{p1}}\right) & \text{dla} \quad \varepsilon_{\text{p1}} < \varepsilon_{\text{p}} \le \varepsilon_{\text{p2}} \end{cases} \tag{10}$$

Taking the failure criterion in the form of ω=1, we obtain:

$$\omega_{\text{creep}} = \Delta\omega_{\text{creep1}} + \Delta\omega_{\text{creep2}} = \left(\frac{K}{\sigma_{\text{c}}}\right)^{n_\omega} \frac{A_\omega}{\left(nn_\omega + 1\right)} \left(\varepsilon_{\text{p1}}\right)^{\left(nn_\omega + 1\right)} + A_\omega \left(\frac{\sigma_{\text{creep}}}{\sigma_{\text{c}}}\right)^{n_\omega} \left(\varepsilon_{\text{p2}} - \varepsilon_{\text{p1}}\right) = 1. \tag{11}$$

In the case where ε_{p1}=0:

$$\omega_{\text{creep}} = \Delta\omega_{\text{creep2}} = A_\omega \left(\frac{\sigma_{\text{creep}}}{\sigma_{\text{c}}}\right)^{n_\omega} \varepsilon_{\text{p2}} = 1. \tag{12}$$

Using the results of experimental tests (Section 2.2), parameters A_ω and n_ω were determined, under the assumption that they are dependent only on the temperature at which the creep process was performed. The values of parameters K and n were determined by approximation using equation (3a) of the results of monotonic tensile tests of the material at elevated temperature (Tab. 2). Knowing the value of the aforementioned parameters, the value of the damage state variable was determined for different creep pre-deformation histories, given in Table 4. It should be emphasized that the proposed model is applicable solely to a σ_{creep} value above transitional stress σ_t.

Tab. 4. The values of the model parameters and the values of the damage state variable for material with different creep pre-deformation histories.

predeformation temperature [°C]	A_ω	n_ω	ε_s or ε_t [%]	$\Delta\omega_{creep1}$	$\Delta\omega_{creep2}$	$\omega_{creep}=\Delta\omega_{creep1}+\Delta\omega_{creep2}$
100	8.21	12.46	ε_s=10	0.198	0.248	0.446
			ε_t=15	0.198	0.615	0.812
200	8.29	1.51	ε_s=0.6	0	0.023	0.023
			ε_t=2.3	0	0.090	0.090
300	4.01	0.51	ε_s=0.4	0	0.010	0.010
			ε_t=2.3	0	0.059	0.059

4.2. Low-cycle fatigue (LCF) loadings

In the case of cyclic loads in the LCF range, it is assumed that, in every cycle, the increase in damage state variable ω_{LCF} is described by a dependency analogous to (4) i.e.:[72,60]

$$\Delta\omega_{LCF}=\int_{\omega_{LCFp}}^{\omega_{LCFk}} d\omega_{LCF}=\frac{A_\omega}{\sigma_c^{n_\omega}}\int_0^{\varepsilon_{p\max}}\sigma^{n_\omega}d\varepsilon_p, \tag{13}$$

where ω_{LCFp}, ω_{LCFk} – respectively, the initial and final value of damage state variable ω_{LCF} in the loading cycle, and after accounting for the dependency describing the cyclic strain curve (3b):

$$\Delta\omega_{LCF}=A_\omega\left(\frac{K'}{\sigma_c}\right)^{n_\omega}\int_0^{\varepsilon_{p\max}}\varepsilon_p^{\,n'n_\omega}d\varepsilon_p\ , \tag{14}$$

$$\Delta\omega_{LCF}=\left(\frac{K'}{\sigma_c}\right)^{n_\omega}\frac{A_\omega}{(n'n_\omega+1)}\varepsilon_{p\max}^{(n_\omega n'+1)}. \tag{15}$$

Accepting that:

$$\varepsilon_{\mathrm{pmax}} = \varepsilon_{\mathrm{ap}}, \quad C = \left(\frac{K'}{\sigma_{\mathrm{c}}}\right)^{n_\omega} \frac{A_\omega}{(n' n_\omega + 1)} \quad \text{and} \quad m = -\frac{1}{n' n_\omega + 1}, \tag{16}$$

we obtain:

$$\Delta\omega_{\mathrm{LCF}} = C\varepsilon_{\mathrm{ap}}^{-\frac{1}{m}}. \tag{17}$$

Using fracture criterion ω_{LCF}=1 and the linear damage accumulation hypothesis, we have:

$$N_{\mathrm{f}} \Delta\omega_{\mathrm{LCF}} = N_{\mathrm{f}} C\varepsilon_{\mathrm{ap}}^{-\frac{1}{m}} = 1, \tag{18}$$

where N_{f} – number of cycles to failure.

If we take a logarithm of the dependency above, we obtain:

$$\log\varepsilon_{\mathrm{ap}} = \log D + m \log N_{\mathrm{f}} \tag{19}$$

where:

$$D = C^m. \tag{20}$$

It should be noted that the dependency above has a similar character to the Manson-Coffin equation (2):

$$\log\varepsilon_{\mathrm{ap}} = \log\varepsilon'_{\mathrm{f}} + c \log N_{\mathrm{f}} \qquad \text{or} \qquad \varepsilon_{\mathrm{ap}} = \varepsilon'_{\mathrm{f}} \left(N_{\mathrm{f}}\right)^c. \tag{21}$$

Comparing dependencies (20) and (21), we obtain:

$$\varepsilon'_{\mathrm{f}} = C^m \quad \text{and} \quad c = m. \tag{22}$$

Parameters $\varepsilon'_{\mathrm{f}}$, c for as-received and material with different pre-deformation histories are presented in Table 4. In turn, parameters A_ω and n_ω were determined using equations (16) and (22):

$$n_\omega = -\frac{c+1}{n'c}, \qquad A_\omega = \left(\varepsilon'_{\mathrm{f}}\right)^{\frac{1}{c}} \left(\frac{\sigma_{\mathrm{c}}}{K'}\right)^{n_\omega} \left(n' n_\omega + 1\right), \tag{23}$$

and their values are given in Table 5. Using the obtained values of the aforementioned parameters and equation (18), the predicted number of cycles to failure $N'_{\mathrm{f\_pred}}$ were determined for different values of the total strain amplitude (Tab. 5, Fig. 11a). It is easy to note that the highest prediction error amounts to 43% and appears only for strain amplitude ε_{a}=0.005. All predicted values fall within the ±50% scatter band.

4.3. Interaction of damages caused by creep and fatigue of material

In the case of material with pre-deformation at elevated temperature, it was proposed for the resultant of the damage state variable ω_{total} to be treated as the sum of damage due to creep ω_{creep} and damage ω_{LCF} resulting from the action of LCF loads:

$$\omega_{\text{total}} = \omega_{\text{creep}} + \omega_{\text{LCF}}. \tag{24}$$

The failure criterion remains unchanged, i.e.:

$$\omega_{\text{total}} = 1. \tag{25}$$

Then, at the moment of total damage, according to (25):

$$\omega_{\text{LCF}} = 1 - \omega_{\text{creep}}. \tag{26}$$

Here, two approaches were considered. In the first, it was assumed that parameters A_ω and n_ω of the damage accumulation model (13) are the same as for undamaged material (Tab. 5). Parameters K' and n' were accepted as for material with the appropriate pre-deformation (Tab. 2). The number of cycles to failure predicted according to this approach is denoted by $N'_{\text{f\_pred}}$. In the second approach, it was proposed for parameters A_ω and n_ω to be determined independently for material with different pre-deformations. Equation (18) then takes on the form of:

$$N_{\text{f}} \Delta\omega_{\text{LCF}} = N_{\text{f}} C \varepsilon_{\text{ap}}^{-\frac{1}{m}} = 1 - \omega_{\text{creep}}. \tag{27}$$

After taking the logarithm of both sides, we obtain, analogously to (19):

$$\log \varepsilon_{\text{ap}} = \log D_1 + m \log N_{\text{f}}, \tag{28}$$

where:

$$D_1 = \varepsilon'_{\text{f}} = \left(\frac{C}{1 - \omega_{\text{creep}}} \right)^m, \tag{29}$$

and m remains unchanged. It is easy to note that, in the case where ω_{creep}=0, i.e. we are dealing with the as-received material, constant D_1=D and equation (28) is identical to (19).

The n_ω parameter determined according to this approach is not subject to change compared to determination by equation (23), and parameter A_ω depends on pre-deformation ω_{creep} obtained during the creep process:

$$A_{\omega} = \left(\varepsilon'_{\mathrm{fl}}\right)^{\frac{1}{c_1}} \left(\frac{\sigma_{\mathrm{c}}}{K'}\right)^{n_{\omega}} \left(n' n_{\omega} + 1\right)\left(1 - \omega_{\mathrm{creep}}\right). \tag{30}$$

The number of cycles to failure predicted according to this approach is denoted by $N_{\mathrm{f\_pred}}$. The results of calculations of the predicted number of cycles until failure with the application of both approaches are presented in Figures 11 and 12 and in Table 5. The table shows the average number of cycles to failure N_{f} obtained in the experiment, and figures show all three points for each strain amplitude ε_{a} level. The application of identical A_{ω} and n_{ω} parameters for the as-received material and material with pre-deformation gives results burdened by a significant error. This pertains, in principle, to all cases of pre-deformation. In the case of preliminary creep at 100°C, this error was associated, above all, with substantial mechanical hardening of the material with respect to the initial material. The effect of temperature is of no greater significance here. In turn, pre-deformation at higher temperatures is associated, above all, with microstructure evolution. And it is precisely changes at the grain level that have a significant impact on the material's mechanical properties, particularly on the cyclic hardening curve, and on the later process of damage accumulation over the course of fatigue. Hence, it is necessary to determine the parameters of the proposed model independently for every pre-deformation history.

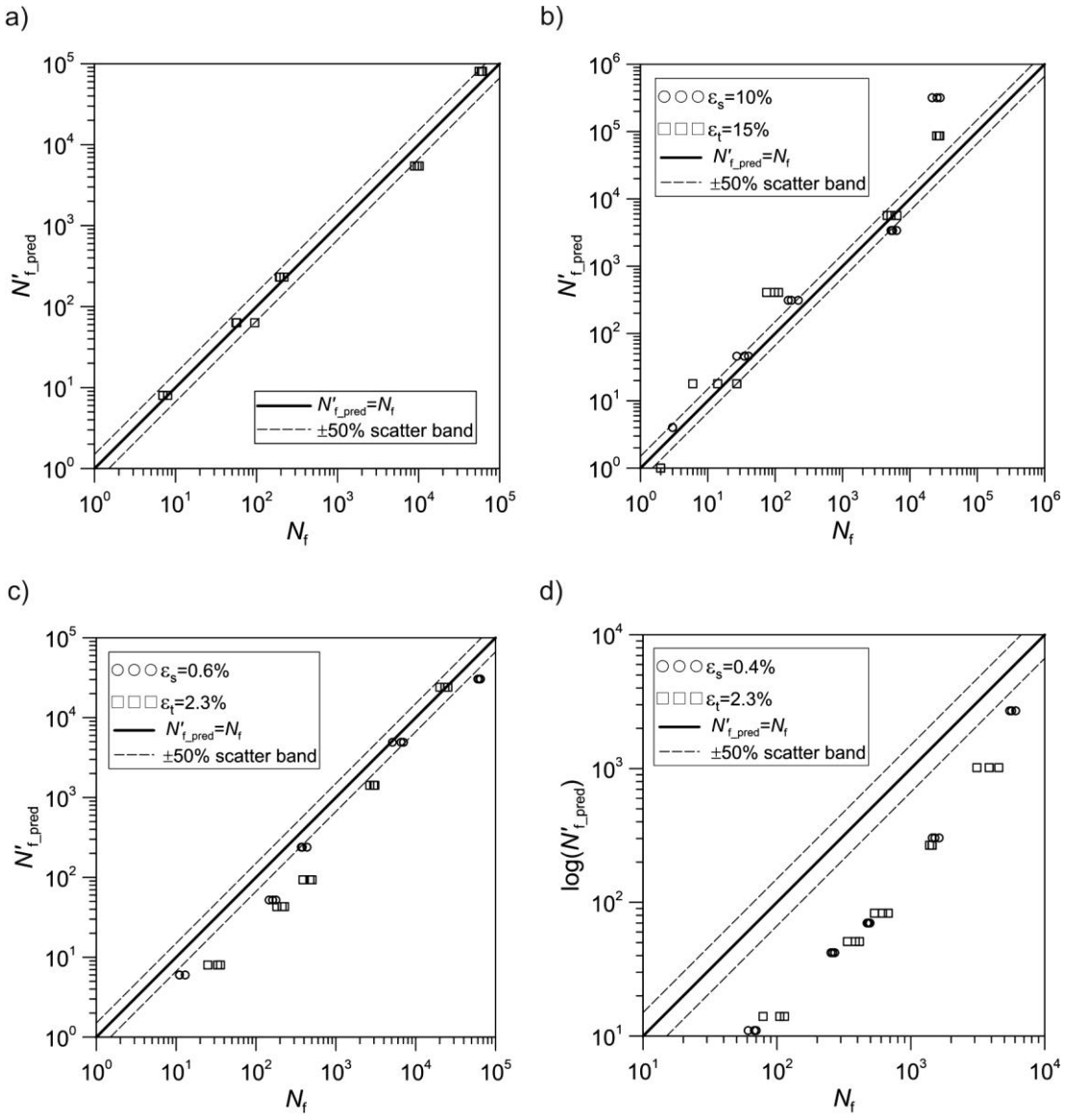

Fig. 11. Predicted N'_{f_pred} vs experimental N_f number of cycles to failure for: a) as-received material and for material with different pre-deformation histories: b) 100°C, c) 200°C, d) 300°C with a marked 50% scatter band.

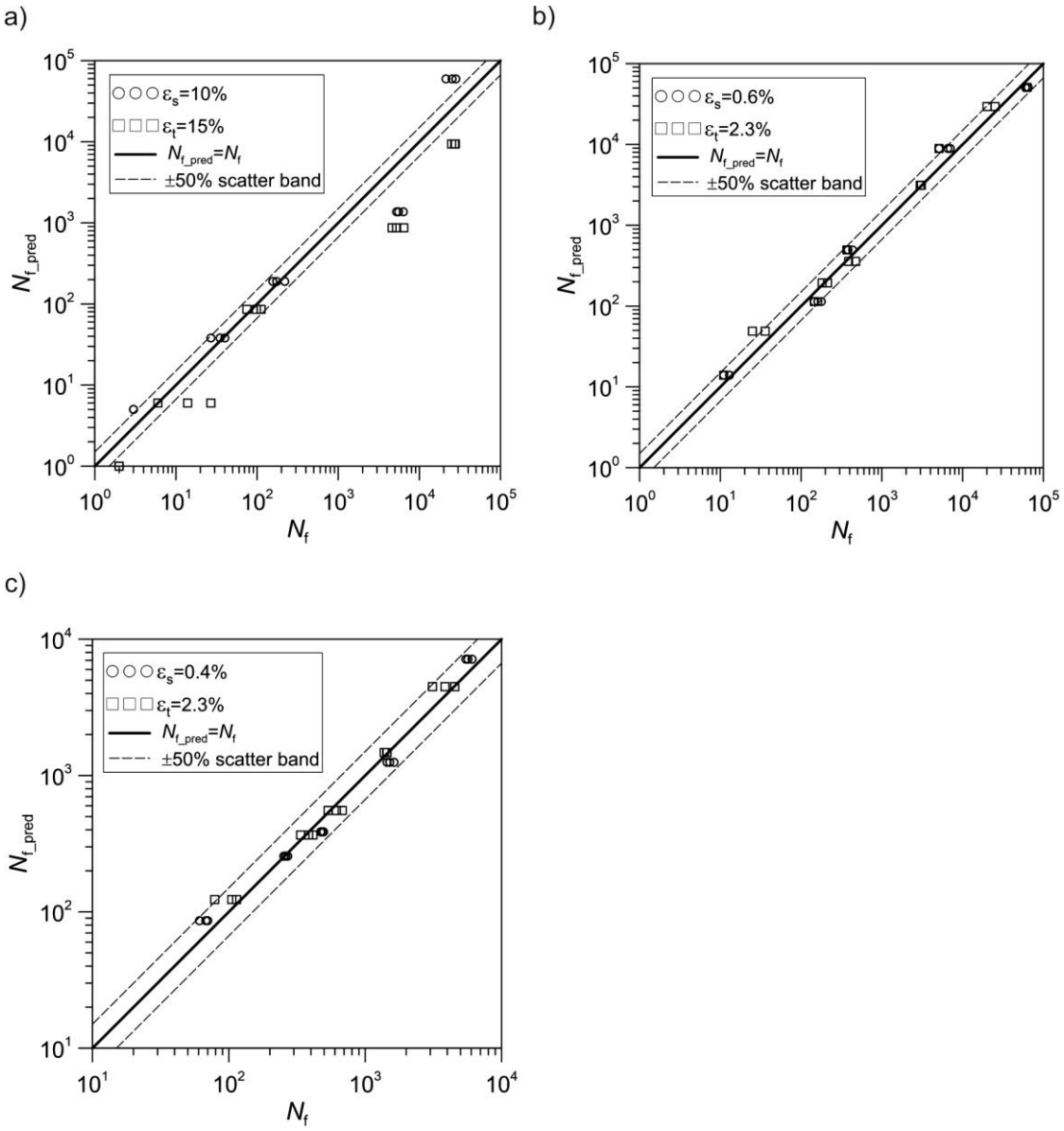

Fig. 12. Predicted N_{f_pred} vs experimental N_f number of cycles to failure for material with different pre-deformation histories: a) 100°C, b) 200°C, c) 300°C with a marked 50% scatter band.

Tab. 5. Experimental N_f and predicted N'_{f_pred} and N_{f_pred} number of cycles to failure for as–received material and for material with different pre-deformation histories together with the values of ε_a.

predef. temp. [°C]	ε_s lub ε_t [%]	A_ω	n_ω	ε_a	N_f (averaged)	N_{f_pred}	N'_{f_pred} (A_ω i n_ω for as-received material)	$\frac{N_f - N_{f\_pred}}{N_f}100\%$	$\frac{N_f - N'_{f\_pred}}{N_f}100\%$
as-received	as-received	13.40	4.216	0.02	7	–	8	–	14
				0.01	69		63		9
				0.008	202		231		14
				0.005	9576		5459		43
				0.0035	58965		80564		37
100	ε_s=10	10.207	2.122	0.02	3	5	4	67	33
				0.01	34	38	46	12	35
				0.008	183	189	312	3	70
				0.005	6294	1366	3383	78	46
				0.0035	24980	59730	319862	139	118
	ε_t=15	32.183	2.681	0.02	2	1	1	50	50
				0.01	16	6	18	63	13
				0.008	95	86	408	9	329
				0.005	5423	867	5685	84	5
				0.0035	26707	9390	86382	65	223
200	ε_s=0.6	5.745	3.749	0.02	12	14	6	17	50
				0.01	162	114	52	30	68
				0.008	395	494	239	25	39
				0.005	6235	8897	4925	43	21
				0.0035	62739	50748	30433	19	51
	ε_t=2.3	1.741	1.434	0.02	31	49	8	58	74
				0.01	208	193	43	7	79
				0.008	455	358	93	21	80
				0.005	2906	3120	1424	7	51
				0.0035	22914	29441	23974	28	5
300	ε_s=0.4	0.984	1.300	0.02	66	86	11	30	83
				0.01	261	256	42	2	84
				0.008	483	387	70	20	86
				0.005	1528	1247	303	18	80
				0.0035	5747	7135	2697	24	53
	ε_t=2.3	0.890	2.046	0.02	99	123	14	24	86
				0.01	379	366	51	3	87
				0.008	610	554	83	9	86
				0.005	1420	1472	267	4	81
				0.0035	3836	4494	1016	17	74

5. Summary and conclusions

This paper presents the results of creep rupture, preliminary creep and LCF tests performed on EN-AW 2024 aluminum alloy. Based on the results of these research, a damage growth model was proposed for both: the creep process and the LCF process as well as for the interaction of creep damage and fatigue damage. The results of experiment together with theoretical and numerical analysis allowed for the formulation of the following conclusions:

1. The existence of a certain transitional value σ_t of creep stress σ_{creep} was observed, above which strain at failure increases as the creep stress value decreases. Reduction of the σ_{creep} value below σ_t results in a decrease in strain at failure.
2. The fatigue life is subject to significant improvement due to preliminary creep, but only in the area where ductile strains are dominant. In the case of lower plastic strains, fatigue life is reduced with respect to that of the as-received material. This tendency, being an effect of recrystallization of the microstructure, is particularly distinct in the case of material after pre-deformation at 300°C.
3. In a model the damage state variable was made dependent on the value of nominal axial stress and growth of axial plastic strain. This approach allowed to obtain a good consistency of experimental results with numerical prediction. This applies to the creep process, the LCF process and the interaction of damage accumulated during creep and subsequent LCF of the material.
4. In fact, the material's microstructure evolves during creep or fatigue at elevated temperature, and because of this, the parameters of the damage accumulation numerical model should also not be constant. The problem here is to identify those dependencies on temperatures, load value and time on the basis of experimental tests. This will be the subject of further research in the field of creep and fatigue processes at elevated temperature.

Acknowledgements:

This research was funded by two sources: (1) Program of the Ministry of Science and Higher Education (Poland) under the name "Regional Initiative of Excellence" in the years 2019–2022 (Project Number: 011/RID/2018/19); (2) the Ministry of Science and Higher Education of Poland within the framework of research project No 2018/29/B/ST8/00697 (National Science Centre of Poland) and realized in Bialystok University of Technology.

References

1. Li H, Xu W, Wang Z, Fang B, Song R, Zheng Z. Effects of re-ageing treatment on microstructure and tensile properties of solution treated and cold-rolled Al–Cu–Mg alloys. *Mater Sci Eng A*. 2016;650: 254-263.
2. Lin YC, Jiang Y-Q, Xia Y-C, Zhang X-C, Zhou H-M, Deng J. Effects of creep-aging processing on the corrosion resistance and mechanical properties of an Al–Cu–Mg alloy. *Mater Sci Eng A*. 2014;605: 192–202.
3. Moy CKS, Weiss M, Xia J, Sha G, Ringer SP, Ranzi G. Influence of heat treatment on the microstructure, texture and formability of 2024 aluminium alloy. *Mater Sci Eng A*. 2012;552: 48–60.
4. Shahsavaria A, Karimzadeha F, Rezaeiana A, Heydari H. Significant increase in tensile strength and hardness in 2024 aluminum alloy by cryogenic rolling. *Proc Mater Sci.* 2015;11: 84 – 88.
5. Cepeda-Jiménez CM, Ruano OA, Carsi M, Careño F. Study of hot deformation of an Al-Cu-Mg alloy using processing maps and microstructural characterization, *Mater Sci Eng A*. 2012;552: 530–539.
6. Lin YC, Xia Y-C, Chen M-S, Jiang Y-Q, Li LT. Modeling the creep behavior of 2024-T3 Al alloy. *Comput Mater Sci.* 2013;67: 243–248.
7. Maximov JT, Duncheva GV, Anchev AP, Ichkova MD. Modeling of strain hardening and creep behavior of 2024T3 aluminium alloy at room and high temperatures. *Comput Mater Sci.* 2014;83: 381-393.
8. Zhang J, Yang S, Lin J. A nonlinear continuous damage model based on short-crack concept under variable amplitude loading. *Fatigue Fract Eng Mater Struct.* 2016;39: 79–94.
9. Amrouche A, Mesmacque G, Garcia S, Talha A. Cold expansion effect on the initiation and propagation of the fatigue crack. *Int. J Fatigue*. 2003;25: 949-54.
10. Warner JJ, Clark PN, Hoeppner DW. Cold expansion effects on cracked fastener holes under constant amplitude and spectrum loading in the 2024-T351 aluminum alloy. *Int J Fatigue.* 2014;68: 209-216.
11. Chakherlou TN, Aghdam AB, Akbari A, Saeedi K. Analysis of cold expanded fastener holes subjected to short time creep: Finite element modelling and fatigue tests. *Mater Des.* 2010;31: 2858-2866.
12. Ma YW, Choi JW, Yoon KB. Change of anisotropic tensile strength due to amount of severe plastic deformation in aluminum 2024 alloy. *Mater Sci Eng A.* 2011;529: 1-8.
13. Figueiredo RB, de Moraes Costa AL, Andrade SM, Aguilar MTP, Cetlin PR. Microstructure and mechanical properties of Pb-4%Sb alloy processed by equal channel angular pressing. *Mater Res.* 2006;9: 101-106.
14. Nagakawa J, Murase Y, Yamamoto N, Fukuzawa T. Irradiation creep at 60°C in SUS 316 and its impact on fatigue fracture. *J Nucl Mater.* 283-287: 397-395.
15. Heath-Smith JR, Kiddle FE. Influence of ageing and creep on fatigue of structural elements in an Al 6% Cu alloy. In: *Thermal and High Strain Fatigue*, Metals and Metallurgy Trust of the Institute of Metals and the Institution of Metallurgists 1976: 391-415.
16. Kiddle FE. Influence of prior heat and creep on fatigue in structural elements of DTD 5014 (RR58) Aluminium alloy. Aeronautical Research Council, Current Papers 1977; No. 1375, Her Majesty's Stationery Office, London.
17. Tomczyk A, Seweryn A. Fatigue life of EN AW-2024 alloy accounting for creep pre-deformation at elevated temperature. *Int J Fatigue*, 2017;103: 488–507.
18. Tomczyk A, Seweryn A, Grądzka-Dahlke M. The effect of dynamic recrystallization on monotonic and cyclic behaviour of Al-Cu-Mg alloy, *Materials*. 2018;11: 874.
19. Rabotnov YN. *Creep Problems in Structure Members*. North-Holland: Amsterdam, 1969.

20. Kachanov LM. Time of the rupture process under creep conditions. Izv Akad Nauk SSR Otd Tech Nauk, 1958;8: 26–31.
21. Yatomi M, Nikbin KM, O'Dowd NP. Creep crack growth prediction using a damage based approach. *Int J Press Vess Pip.* 2003;80: 573–83.
22. Tabuchi M, Hongo H, Li YK, Watanabe T, Takahashi Y. Evaluation of microstructures and creep damages in the HAZ of P91 steel weldment. *J Press Vess Technol.* 2009;131: 021406-1–6-6.
23. Chen LY, Wang GZ, Tan JP, Xuan FZ, Tu ST. Effects of residual stress on creep damage and crack initiation in notched CT specimens of a Cr-Mo-V steel. *Eng Fract Mech.* 2013;97: 80–91.
24. Pettinà M, Biglari F, Heaton A, Brown P, Nikbin K. Modelling damage and creep crack growth in structural ceramics at ultra-high temperatures. *J Eur Ceram Soc.* 2014;34: 2799–805.
25. Zhao L, Alang N, Nikbin K. Investigating creep rupture and damage behaviour in notched P92 steel specimen using a microscale modelling approach. *Fatigue Fract Eng Mater Struct.* 2018;41: 456–472.
26. Shlyannikov V, Tumanov A. Creep damage and stress intensity factor assessment for plane multi-axial and three-dimensional problems. *Int J Sol Struct.* 2018;150: 166-183.
27. Othman AM, Dyson BF, Hayhurst DR, Lin J. Continuum damage mechanics modelling of circumferentially notched tension bars undergoing tertiary creep with physically-based constitutive equations. *Acta Metal Mater.* 1994;42: 597–611.
28. Kowalewski ZL, Hayhurst DR, Dyson BF. Mechanisms-based creep constitutive equations for an aluminium alloy. *J Strain Anal Eng Des.* 1994;29: 309–16.
29. Mustata R, Hayhurst RJ, Hayhurst DR, Vakili-Tahami F. CDM predictions of creep damage initiation and growth in ferritic steel weldments in a medium-bore branched pipe under constant pressure at 590 C using a four-material weld model. *Arch Appl Mech.* 2006;75: 475–95.
30. Pétry C, Lindet G. Modelling creep 27ehavior and failure of 9Cr-0.5Mo-1.8W-VNb steel. *Int J Press Vess Pip.* 2009;86: 486–94.
31. Hosseini E, Holdsworth SR, Mazza E. Stress regime-dependent creep constitutive model considerations in finite element continuum damage mechanics. *Int J Damage Mech.* 2013;22: 1186–1205.
32. Miner MA. Cumulative damage in fatigue. *J Appl Mech.* 1945;12A1: 59-64.
33. Kim J-H, Lee D-C, Lee J-H, Ham Y-S, Kang K-W. Fatigue Analysis of Spot-Welded Automobile Components Considering Fatigue Damage-Induced Stiffness Degradation in Time and Frequency Domains. *Int J Prec Eng Manufact.* 2017;18: 389-397.
34. Liu Q, Shi W., Chen Z. Rubber fatigue life prediction using a random forest method and nonlinear cumulative fatigue damage model. *J Appl Polym Sci.* 2020;137: 48519.
35. He L, Akebono H, Sugeta A, Hayashi Y. Cumulative fatigue damage of stress below the fatigue limit in weldment steel under block loading. *Fatigue Fract Eng Mater Struct.* 2020;43: 1419–1432.
36. Kurek M, Łgoda T. Fatigue damage cumulation in materials under random loading based on an energy model. *Fatigue Fract Eng Mater Struct.* 2021;44: 1114–1124.
37. Macek W, Branco R, Domingos Costa J, Pereira C. Strain sequence effect on fatigue life and fracture surface topography of 7075-T651 aluminium alloy. *Mech Mater.* 2021;160: 103972.
38. Kumar J, Rao AV, Kumar V. Simulation of elevated temperature fatigue damage evolution using the finite element method for near alpha titanium alloy. *Fatigue Fract Eng Mater Struct.* 2015;38: 466–474.
39. Carrascal IA, Casado JA, Diego S, Polanco JA, Gutierrez-Solana F. Fatigue damage analysis based on energy parameters in reinforced polyamide. *Fatigue Fract Eng Mater Struct.* 2012;35: 683–691.

40. Ellyin F, Golos K, Xi Z. In-Phase and Out-of-Phase Multiaxial Fatigue. *J Eng Mater Technol*. 1991;113:112-118
41. Xia Z, Kujawski D, Ellyin F. Effect of mean stress and ratcheting strain on fatigue life of steel. *Int J Fatigue.* 1996;18: 335–341.
42. Ahmadzadeh GR, Varvani-Farahani A. Concurrent ratcheting–fatigue damage analysis of uniaxially loaded A-516 Gr.70 and 42CrMo Steels. *Fatigue Fract Eng Mater Struct.* 2012;35: 962–970.
43. Łagoda T, Macha E. Generalization of energy-based multiaxial fatigue criteria to random loading. In: Kalluri S, Bonacuse PJ, eds. *Multiaxial Fatigue and Defromations: Testing and Prediction 2000*, West Conshohocken PA: ASTM STP;1387: 173-190.
44. Macha E, Niesłony T. Critical plane fatigue life models of materials and structures under multiaxial stationary random loading: the state of the art in Opole Reasearch Centre CESTI and directions of future activities. *Int J Fatigue.* 2012;39: 95-102.
45. Ahmadzadeh GR, Varvani-Farahani A. Fatigue damage and life evaluation of SS304 and Al 7050-T7541 alloys under various multiaxial strain paths by means of energy-based Fatigue damage models. *Mech Mater.* 2016;98: 59–70.
46. Szusta J, Seweryn A. Damage accumulation modeling under uniaxial low cycle fatigue at elevated temperatures. *Eng Failure Anal.* 2015;56: 474–483.
47. Szusta J, Seweryn A. Fatigue damage accumulation modelling in the range of complex low-cycle loadings – The strain approach and its experimental verification on the basis of EN AW-2007 aluminum alloy. *Int J Fatigue*. 2011;33: 255–264.
48. Hormozi R, Biglari F, Nikbin K. Taguchi sensitivity analysis of damage parameters for predicting the damage Mechanism of 9Cr steel under low-cycle fatigue test. *Fatigue Fract Eng Mater Struct.* 2014;37: 1211–1222.
49. Zhang L-H, Shang D-G, Liu X-D, Sun Y-J, Guo Y-B, Liu F-Z, Chen T. A nonlinear fatigue damage-healing model for copper film by LSP. *Fatigue Fract Eng Mater Struct.* 2014;37: 1232–1241.
50. Du W, Luo Y, Wang Y, Chen S, Yu D. A new energy-based method to evaluate low-cycle fatigue damage of AISI H11 at elevated temperature. *Fatigue Fract Eng Mater Struct.* 2017;40: 994–1004.
51. Ma L, Luo Y, Wang Y, Du W, Zhang J. Constitutive and damage modelling of H11 subjected to low-cycle fatigue at high temperature. *Fatigue Fract Eng Mater Struct.* 2017;40: 2107–2117.
52. Smith KN, Watson, Topper TH. A stress strain function for the fatigue of metals. *J Mater.* JMLSA 1970;5: 767–778.
53. Tanegashima R, Ohara I, Akebono H, Kato M, Sugeta A. Cumulative fatigue damage evaluations on spot-welded joints using 590MPa-class automobile steel. *Fatigue Fract Eng Mater Struct.* 2015;38: 870–879.
54. De Palma V, Tomasella A, Frendo F, Melz T, Sonsino CM. Analysis of different fatigue damage accumulation theories and damage parameters based on experiments with the steel HC340LA. *Mat-wiss u Werkstofftech.* 2016;47: 116-1173.
55. Correia JAFO, Raposo P, Muniz-Calvente M, Blasón S, Lesiuk G, De Jesus AMP, Moreira PMGP, Calçada RAB, Canteli AF. A generalization of the fatigue Kohout-Věchet model for several fatigue damage parameters. *Eng Fract Mech.* 2017;185: 284–300.
56. Lemaitre J, Chaboche JL. *Mechanics of Solid Materials*. Cambridge University Press, Cambridge, 1994.
57. Warhadpande A, Sadeghi F, Michael NK, Doll G. Effects of plasticity on subsurface initiated spalling in rolling contact fatigue. *Int J Fatigue.* 2012;36: 80–95.
58. Huang Z-Y, Wagner D, Bathias C, Chaboche JL. Cumulative fatigue damage in low cycle fatigue and gigacycle fatigue for low carbon–manganese steel. *Int J Fatigue.* 2011;33: 115–121.

59. Bhatti NA, Wahab MA. Fretting fatigue damage nucleation under out of phase loading using a continuum damage model for non-proportional loading. *Tribol Inter.* 2018;121: 204–213.
60. Tomczyk A, Seweryn A. Experimental investigation and modeling of damage accumulation of EN-AW 2024 aluminum alloy under creep condition at elevated temperature. *Materials*. 2021;14: 404.
61. Tomczyk A, Seweryn A, Doroszko M. Monotonic behaviour of typical Al-Cu-Mg alloy pre-strained at elevated temperature. *J Theor Appl Mech.* 2018;56: 1055–1068.
62. Tomczyk A, Koniuszewski R. Construction of a system for measuring sample elongations at elevated temperatures using 520 devices intended for work at room temperature. Patent No. PL 68955 Y1 2017 (in Polish).
63. EN ISO 204, 2009, Metallic materials, uniaxial creep testing in tension: Method of test.
64. ASTM E606, 2012, Standard Test Method for Strain-Controlled Fatigue Testing
65. Li L-T, Lin YC, Zhou H-M, Jiang Y-Q. Modeling the high-temperature creep behaviors of 7075 and 2124 aluminum alloys by continuum damage mechanics, *Comp Mater Sci.* 2013;73: 72–78.
66. Manson SS. Behavior of materials under conditions of thermal stress. National Advisory Committee for Aeronautics. Report No. NACA TN-2933, 1954.
67. Coffin LF. A study of the effect of cyclic thermal stresses on a ductile metal. *Trans ASME*. 1954;76: 931–50.
68. Basquin OH. The exponential law of endurance tests. *ASTM Proc.* 1910;10: 625–30.
69. Ramberg W, Osgood W. Description of Stress–Strain Curves by Three Parameters. NASA Scientific and Technical Information Facility 1943, Washington, p. 902.
70. Sakai T, Belyakov A, Kaibyshev R, Miura H, Jonas JJ. Dynamic and post-dynamic recrystallization under hot, cold and severe plastic deformation conditions. *Prog Mater Sci.* 2014;60: 130-207.
71. Sitdikov O, Sakai T, Goloborodko A, Miura H, Kaibyshev R. Grain refinement in coarse-grained 7475 Al alloy during severe hot forging. *Philos Mag.* 2005;85: 1159–75.
72. Falkowska A, Seweryn A, Szusta J. Predicting the fatigue strength and life of 316L steel sinters of varying porosity for implants in a uniaxial loading state. *Eng Fract Mech.* 2018;200: 146–165.

Highlights

- experimental on creep-rupture, creep and LCF tests of AN-EW 2024 aluminum alloy
- a simply model for damage growth during creep at elevated temperature
- modeling of fatigue damage accumulation for as-received and pre-deformed material
- verification of LCF damage growth model using experimental data